EXTRACTING ROTOR INDUCED & PROFILE POWER FROM CFD — A PROOF-OF-CONCEPT STUDY

Albert Abraham
Penn State University
University Park, PA, USA

Pierce Hart
Penn State University
University Park, PA, USA

Sven Schmitz
Penn State University
University Park, PA, USA

ABSTRACT

The present paper introduces a novel methodology to extract rotor induced and profile power from high-fidelity computational aerodynamics simulations. The methodology is based on partial pressure fields which split the static pressure of a numerical Navier-Stokes solution into equivalent Euler and dissipative partial pressure fields. Here the original formulation is extended and applied to rotating reference frames. Test cases include the two-bladed Knight & Hefner rotor in slow axial climb at variable blade collective as well as the ONERA HAD-1 propeller in axial flight. Quantitative comparisons of rotor power breakdown are conducted against results obtained from blade-element momentum theory. It is found that the novel methodology based on partial pressure fields gives promising results towards a complete near-field power breakdown of high-fidelity computational aerodynamics simulations of rotating systems.

NOTATION

*

Symbols

a Local speed of sound

c_d Local drag coefficient

c_l Local lift coefficient

c_p Static pressure coefficient

c_{p_E} Euler pressure coefficient

c_{p_μ} Dissipative pressure coefficient

F Prandtl tip-loss factor

F_x Tangential force, N

F_z Normal force, N

J Advance ratio

M_∞ Freestream Mach number

N_b Number of blades

p Static pressure field, Pa

p_E Euler (inviscid) partial-pressure, Pa

p_μ Dissipative (viscous) partial-pressure, Pa

S_ϕ Transport equation source term

$\vec{v}$ Absolute velocity vector, m/s

v_c Climb velocity, m/s

v_i Induced velocity, m/s

$\vec{v}_r$ Relative velocity vector, m/s

R Rotor radius, m

Re_{75} Reynolds number at 75% radial station

P_i Induced power, kW

U Local velocity, m/s

α Angle of attack, deg

θ Rotor collective angle, deg

λ Local inflow ratio

λ_c Climb ratio

Ξ Diffusion coefficient

ρ Fluid density, $\frac{kg}{m^3}$

σ Rotor solidity

$\bar{\bar{\tau}}$ Viscous stress tensor

τ_w Wall shear stress, Pa

ϕ Local inflow angle, deg

$\vec{\Omega}$ Reference frame angular velocity, RPM

*

Acronyms

BEMT Blade Element Momentum Theory

CFD Computational Fluid Dynamics

NACA National Advisory Committee for Aeronautics

PPF Partial-pressure Field

INTRODUCTION

In classical rotor aerodynamics, power contributions are often split into induced and profile components. However, in its current state, computational fluid dynamics (CFD) is unable to directly extract these contributions. Instead, blade designers are reliant on traditional full-potential and Euler solutions, as well as prescribed and free-wake vortex methods. Hence, there is a disconnect between viscous/inviscid interaction of the classical methods and state-of-the-art CFD, thus limiting the effectiveness of these tools to improve lower-order design tools based on blade-element momentum theory (BEMT).

Removing this technical barrier will not only advance the fundamental understanding of rotor aerodynamics, but the knowledge gained can improve classical BEMT, full-potential, and free-wake methods that are seeing a re-emergence in current multi-rotor vehicle development. In addition to rotorcraft applications, an understanding of force and power breakdown for fixed-wing aircraft remains a topic of interest, with the capability to break down the separate contributions of drag and thrust proving to be challenging. This topic is also of particular interest for open rotor technology on commercial transport aircraft (Ref. 1). The necessity to better understand the power contributions of rotor blades, and the ability to decompose them into their respective contributions for fixed-wing aircraft in power-on configurations, has led to recent developments in force-bookkeeping methods. So far, two classes of decomposition methods have been extended to rotating frames: thermodynamic decompositions and exergy balance.

Thermodynamic based decompositions are rooted in entropy generation, first demonstrated by Oswatitsch (Ref. 2). The method has become matured through the contributions of van der Vooren and Sloof (Ref. 3), Paparone and Tognaccini (Ref. 4) and Destarac and van der Vooren (Ref. 5). In their work, the authors developed an irreversible velocity field which can be evaluated in the far-field to determine profile drag, with the induced drag solved as a complementary term. Moreover, the method was advanced to prove capable of decomposing wave drag. In the early 2010's, Verley and Méheut demonstrated the applicability of the method in a rotating reference frame (Refs. 6, 7). Simultaneously, research was conducted to apply thermodynamic methodologies to unsteady flows, initially undertaken by Gariépy et al. (Ref. 8) and Toubin et al. (Refs. 9, 10). Recently, Nadal et al. (Ref. 11) extended the latter method to decompose unsteady flows in a rotating reference frame; however, it was concluded that the method falls short as it suggests that all thrust is attributed to a viscous force. As such, no method thus far has proven capable of breaking down induced and profile forces on rotors.

On the other hand, the exergy method matured by Arntz et al. (Refs. 12–14) provides an alternate perspective. This method provides a thorough assessment of force formation in the far-field and can be linked to conventional momentum-based forces. Berhouni et al. (Ref. 15) extended the applicability of the method to the rotating reference frame, with applications to the ONERA HAD-1 propeller as well as turbomachinery applications such as the NASA Rotor 37 (Ref. 16). A recent assessment of the potential of the various methodologies for industrial applications was favorable (Ref. 17).

A conceptually different perspective for the evaluation of forces and power is to decompose them in the near-field. This subject area is the more recent development of Partial-Pressure fields (PPFs) and remains unexplored in a rotating reference frame. Originally developed by Schmitz & Coder, PPFs were applied to steady incompressible flow cases (Ref. 18). This was then extended to the compressible flow regime by Schmitz (Ref. 19), where Hart & Schmitz (Refs. 20, 21) explored applications of the method in subsonic and transonic flows with a particular interest in the bookkeeping of wave drag with a near-field PPF. The method has matured in recent years such that it was applied to more complex configurations (Ref. 22), and more recently the method has been further developed to directly extract wave drag in three-dimensional near-field flows (Ref. 23). The concluding observation is that PPFs are indeed able to bookkeep drag and power contributors. And there are advantages to using near-field methods to decompose drag sources, particularly for highly-integrated configurations with notable interactional aerodynamics. This provides the motivation for the present work. Here the formulation is extended to rotating reference frames in order to apply the methodology to both rotors and propellers. The present paper is a proof-of-concept study with application of the PPF power breakdown methodology to the Knight & Hefner rotor as well as the ONERA HAD-1 propeller. Comparisons are made against an in-house BEMT solution method as a quantitative reference case.

METHODS

Partial-Pressure Fields (PPFs)

The assumptions for the PPF derivation are steady flow, no heat addition, and no body forces. It was shown in prior theoretical work (Ref. 19) that an Euler partial pressure accounts for induced effects, while an associated dissipative partial pressure accounts for blade section form drag. The general momentum equation in the rotating reference frame reads:

$$\nabla \cdot (\rho \vec{v}_r \otimes \vec{v}) + \rho (\vec{\Omega} \times \vec{v}) = -\nabla p + \nabla \cdot \bar{\bar{\tau}} \quad (1)$$

The foundation of the PPF decomposition is rooted in breaking down the static pressure field into an inviscid "Euler" partial-pressure (induced), p_E, and a viscous "dissipative" partial-pressure (form), p_μ, in the following way:

$$p = p_E + p_\mu \quad (2)$$

Applying the definition of the PPFs with the absolute velocity formulation of the momentum equation yields:

$$\nabla p_E = -\nabla \cdot (\rho \vec{v}_r \otimes \vec{v}) - \rho (\vec{\Omega} \times \vec{v}) \quad (3)$$

$$\nabla^2 p_E = -\nabla \cdot \left[\nabla \cdot (\rho \vec{v}_r \otimes \vec{v}) \right] - \nabla \cdot \left[\rho (\vec{\Omega} \times \vec{v}) \right] \quad (4)$$

The elliptic PDE in Eq. (4) is convenient for use in CFD codes that have a built-in Poisson solver. For the purposes of evolving the PPF decomposition method to work in a rotating reference frame in general-purpose CFD codes, a transport equation is formulated according to:

$$\frac{\partial (\rho \phi)}{\partial t} + \rho (\vec{v} \cdot \nabla) \phi = \nabla \cdot (\Xi \nabla \phi) + S_\phi \quad (5)$$

After some manipulation and using Eqs. (3,4), one can formulate the source term, S_ϕ, in Eq. (5) to become:

$$\begin{aligned} S_\phi = -\rho \vec{v} \cdot \left[\nabla \cdot (\rho \vec{v}_r \otimes \vec{v}) \right] + \Xi \nabla \cdot \left[\nabla \cdot (\rho \vec{v}_r \otimes \vec{v}) \right] \\ + \Xi \nabla \cdot \left[\rho (\vec{\Omega} \times \vec{v}) \right] \end{aligned} \quad (6)$$

The general transport equation (5) can then be written as

$$\begin{aligned} \rho (\vec{v} \cdot \nabla) p_E = -\rho \vec{v} \cdot \left[\nabla \cdot (\rho \vec{v}_r \otimes \vec{v}) \right] + \Xi \nabla^2 p_E \\ + \Xi \nabla \cdot \left[\nabla \cdot (\rho \vec{v}_r \otimes \vec{v}) \right] + \Xi \nabla \cdot \left[\rho (\vec{\Omega} \times \vec{v}) \right] \end{aligned} \quad (7)$$

where the diffusion coefficient, Ξ, is a function of both Reynolds number and dynamic viscosity, μ. Equation (7) can thus be solved for the Euler partial pressure, p_E.

In reference to rotor force and power breakdown, sectional rotor thrust is computed from pressure and skin friction at each blade section according to

$$dT_{CFD} = -\oint (p - \tau_w)\, dx\, dr \quad (8)$$

while the partial pressure fields, p_E and p_μ, are used to determine sectional induced and profile torques as:

$$dQ_{CFD} = \underbrace{\oint (-p_E)\, r\, dx\, dr}_{Induced} + \underbrace{\oint (-p_\mu + \tau_w)\, r\, dx\, dr}_{Profile} \quad (9)$$

Equation (9) is the foundation of a CFD rotor force and power breakdown and will be used to compare quantitatively against BEMT reference data introduced in the next section.

Blade Element Momentum Theory (BEMT)

The classical breakdown of rotor induced and profile power is best illustrated in Blade Element Momentum Theory (BEMT). In this section, basic relations are reviewed as they constitute reference values for the proposed PPF power decomposition of this work.

Figure 1 shows a detailed view of a blade section element, including forces, angles, and local velocities. The x-direction is defined in the rotor plane in the direction of the local entrainment speed, Ωr, while the z-direction points upstream in the axial freestream direction; the radial coordinate along the blade is denoted by r.

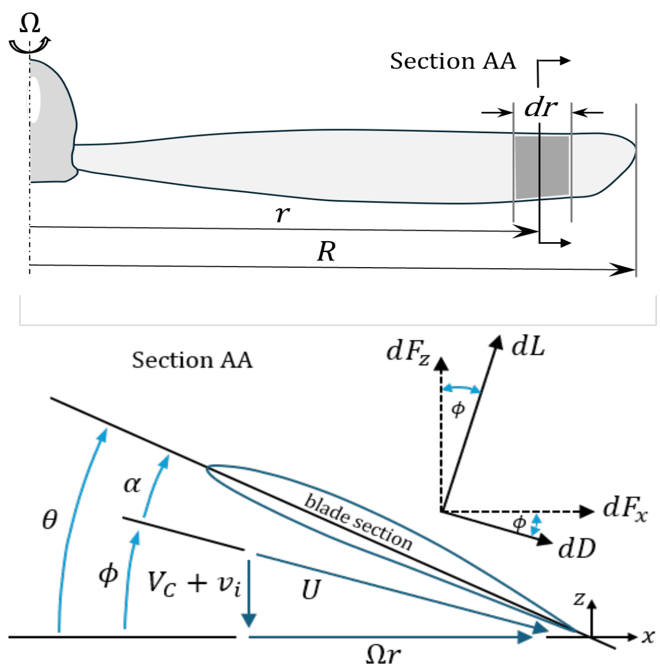

Figure 1. BEMT - Forces on rotor blade section.

The following angle relation applies to each blade section:

$$\Theta = \alpha + \phi \quad (10)$$

Here ϕ is the local inflow angle, and α is the local blade section angle of attack. The local inflow angle is determined by

$$\phi = \tan^{-1} \left(\frac{V_C + v_i}{\Omega r} \right) \quad (11)$$

with $V_C + v_i$ being the local axial (z) velocity component and Ωr being the local entrainment speed (x). In this context, V_C is the climb speed (for a helicopter rotor) or the axial speed (for a propeller), while v_i is the local rotor induced velocity. The total velocity U at a blade section thus becomes:

$$U = \sqrt{(\Omega r)^2 + (V_C + v_i)^2} \quad (12)$$

Subsequently, the local Mach number, Ma, is defined as

$$Ma = \frac{U}{a} \tag{13}$$

where a is the speed of sound. In the BEMT implementation of this work, no airfoil tables are used. Instead, blade section lift and drag coefficients are simply defined according to

$$c_l = \frac{c_{l\alpha}}{\sqrt{1-Ma^2}}(\alpha - \alpha_0) \qquad c_d = c_{d,min} + K\alpha^2 \tag{14}$$

where $c_{l\alpha}$ is the lift-curve slope and α_0 is the zero-lift angle of the local blade section. In Eq. (14), parameters $c_{d,min}$ and K are determined either from data (in case of the Knight & Hefner rotor) or from a Fluent computed airfoil polar at the 75% station (in case of the ONERA HAD-1 propeller).

Note that the lift coefficient, c_l, in Eq. (14) includes a Prandtl-Glauert compressibility correction relevant to the ONERA HAD-1 propeller. Blade element lift and drag forces become

$$dL = \frac{1}{2}\rho U^2 c_l \, cdr \qquad dD = \frac{1}{2}\rho U^2 c_d \, cdr \tag{15}$$

where c is the local blade chord. From Fig. 1, it is apparent how these can be transformed into dF_z and dF_x, respectively.

$$dF_z = dL\cos\phi - dD\sin\phi \qquad dF_x = dL\sin\phi + dD\cos\phi \tag{16}$$

Next, BEMT thrust and torque are defined in x, z directions as:

$$dT_{BEMT} = dF_z \qquad dQ_{BEMT} = dF_x \, r \tag{17}$$

For the purpose of this work, BEMT blade section torque is then split into induced and profile components following:

$$dQ_{BEMT} = \underbrace{dL\sin\phi \; r}_{Induced} + \underbrace{dD\cos\phi \; r}_{Profile} \tag{18}$$

Equation (18) constitutes a BEMT reference case for comparison against CFD computed induced power by means of PPF decomposition according to Eq. (9). The BEMT thrust and torque relations in Eqs. (17-18) require knowledge of the local inflow angle, ϕ, which is typically determined from solving a suitable inflow equation for the local inflow ratio, λ, at each blade section defined according to

$$\lambda = \frac{V_C + v_i}{\Omega R} \tag{19}$$

such that the inflow angle, ϕ, in Eq. (11) can be computed as:

$$\phi = \tan^{-1}\left(\frac{\lambda}{r}\right) \tag{20}$$

In the following, separate inflow equations for λ are derived for the Knight & Hefner and ONERA HAD-1 propeller due to differences in flow states between the two rotors.

Knight & Hefner Rotor In this paper, the two-bladed variant of the classical Knight & Hefner rotor is considered. The original Knight & Hefner experiment was conducted in hover; however, a very low climb ratio of $\lambda_c = V_C/(\Omega R) = 0.04$ close to hover is considered in this work due to the simpler computational setup and boundary conditions in Fluent associated with a small axial freestream flow through the rotor. The rotor blades have a rectangular planform and are equipped with the NACA 0015 airfoil (Ref. 24).

Following the analysis in Leishman (Ref. 25), blade section thrust coefficient from blade-element theory (BET) and momentum theory (MT) are determined as:

$$BET: \qquad dC_T = \frac{1}{2}\sigma c_{l,\alpha}\left(\Theta\left(\tfrac{r}{R}\right)^2 - \lambda\tfrac{r}{R}\right) d\tfrac{r}{R} \tag{21}$$

$$MT: \qquad dC_T = 4F\lambda\left(\lambda - \lambda_C\right)\tfrac{r}{R}\, d\tfrac{r}{R} \tag{22}$$

In Eq. (21), $\sigma = N_b c/\pi R$ is the rotor solidity of the rectangular blade, and F is Prandtl's tip loss factor according to:

$$F = \frac{2}{\pi}\cos^{-1}\left(e^{-\frac{N_b}{2}\frac{1-r/R}{r/R\sin\phi}}\right) \tag{23}$$

Note that in Eq. (21), a small-angle approximation has been used twice with $dC_T \approx dC_l\cos\phi \approx dC_l$ from Eq. (16) and $\phi \approx \lambda/r$ from Eq. (20). Equating (21) and (22) results in the classical inflow equation for helicopter rotors in axial climb:

$$\lambda(r,\lambda_c) = \sqrt{\left(\frac{\sigma c_{l\alpha}}{16F}\right)^2 + \frac{\sigma c_{l\alpha}}{8F}\Theta(r)\frac{r}{R}} - \left(\frac{\sigma c_{l\alpha}}{16F} - \frac{\lambda_c}{2}\right) \tag{24}$$

ONERA HAD-1 Propeller In the present work, the ONERA HAD-1 light propeller is considered as an additional test case for the proposed PPF power decomposition. The CAD geometry for the propeller was provided by ONERA. In contrast to the Knight & Hefner rotor, the ONERA HAD-1 propeller has a variable blade chord and more than thirty degrees of twist and is equipped with several cambered airfoils along the blade. The test case considered is the same as documented in (Ref. 11) with an axial advance ratio of $J = V_C/(\Omega R) = 0.6$ at a tip Mach number of 0.5.

In this context, it is important to note that BEMT propeller inflow violates the small-angle approximation typically used for lightly-loaded helicopters; therefore, a different inflow equation is required for BEMT analysis. Here a more general version than documented in (Ref. 26) is derived where the full force transformation in Eq. (16) is recast into the respective BET equation with an unchanged MT component such that:

$$BET: \quad dC_T = \sigma\left(\frac{U}{\Omega R}\right)^2\left(c_l\cos\phi - c_d\sin\phi\right)\tfrac{r}{R}\, d\tfrac{r}{R} \tag{25}$$

$$MT: \qquad dC_T = 4F\lambda\left(\lambda - \lambda_C\right)\tfrac{r}{R}\, d\tfrac{r}{R} \tag{26}$$

In Eq. (25), the solidity parameter is now locally defined as $\sigma = N_b c/(2\pi r)$ similar to wind turbine aerodynamic theory (Ref. 27). Equating Eqs. (25) and (26) now results in a suitable inflow equation for the ONERA HAD-1 propeller in axial flight, which is solved very efficiently in a few iterations with intial values provided by the simpler inflow equation (24):

$$\lambda(r,\lambda_c) = \sqrt{\sigma\left(\frac{U}{\Omega R}\right)^2 \frac{c_l\cos\phi - c_d\sin\phi}{4F} + \left(\frac{\lambda_c}{2}\right)^2} + \frac{\lambda_c}{2} \tag{27}$$

CFD Grid Generation

The first test rotor used for the force/power decomposition was the classical NACA Knight & Hefner rotor (Ref. 24). This blade was chosen for its simple rectangular, untwisted planform and straightforward comparison against BEMT data. Mesh generation was done in Pointwise. A view of the blade tip shows the structured surface mesh with unstructured end caps along with the volume mesh in Figure 2. The surface grid used for this study consisted of 481 wrap-around points, 250 points along the blade radius, and 6 points to model the blunt trailing edge. The unstructured volume mesh was 6.85 million cells in total and was built to operate at Re_{75} of 180,000 with a surface $y^+ < 2$.

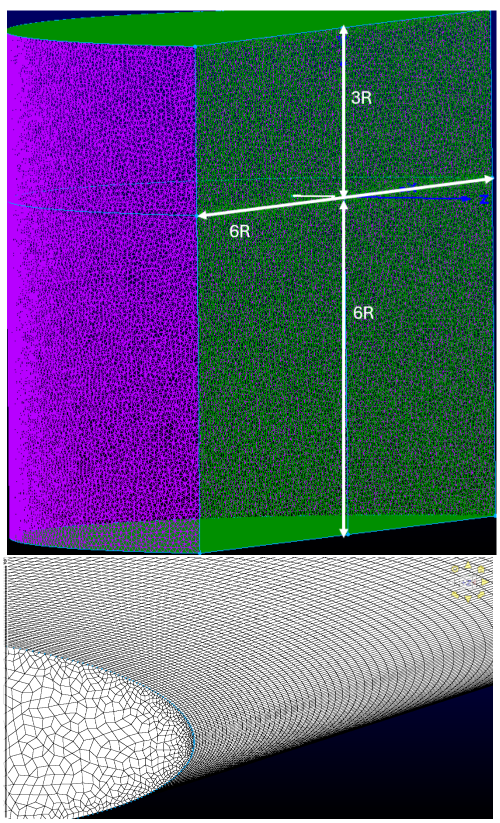

Figure 2. Computational grid - Knight & Hefner rotor.

The second rotor to test the proposed force/power decomposition was the ONERA HAD-1 propeller. A similar mesh generation was conducted in Pointwise. A view of the propeller root shows the structured surface mesh with unstructured end caps along with the volume mesh in Figure 3. The surface grid comprised of 510 wrap-around points, 500 points along the blade radius, and 25 points to model the blunt trailing edge. In total, the unstructured volume mesh was 49 million cells. The grid was designed to operate at Re_{75} of 1,600,000 with a surface $y^+ < 0.75$.

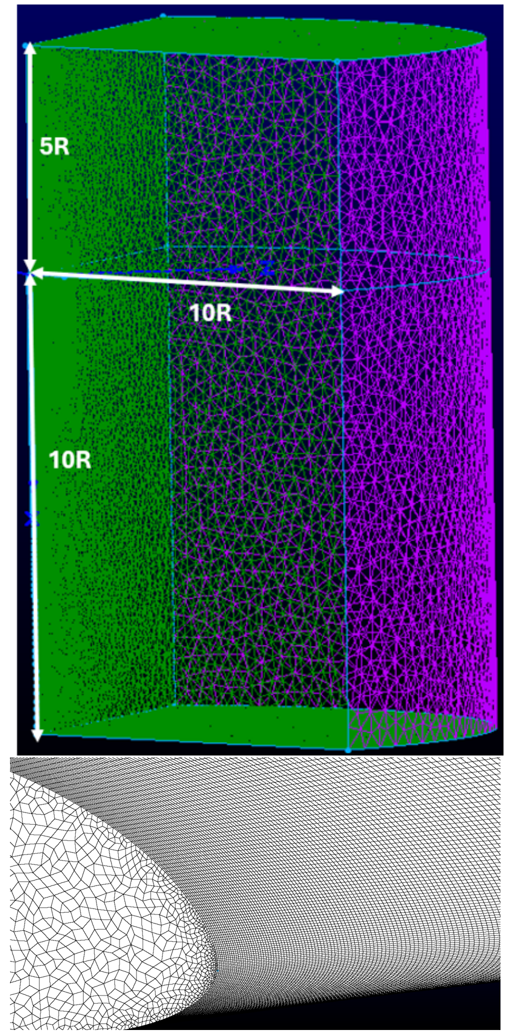

Figure 3. Computational grid - ONERA HAD-1 propeller.

CFD Solver Setup

The commercial ANSYS Fluent 2023 R2 solver was used to run the simulations. All schemes in Fluent were second-order accurate, and gradients were evaluated using the Green-Gauss cell-based method. The absolute velocity formulation was used to account for the rotation of the reference frame. The pressure-based, incompressible solver was used for the Knight & Hefner rotor, and the pressure-based, compressible solver was used for the ONERA HAD-1 propeller. Generalized $k-\omega$ (GEKO) was used for turbulence closure. Only one blade was meshed for both the Knight & Hefner rotor and the ONERA HAD-1 propeller, with periodic boundary conditions used to complete the domains. To implement PPFs into the solver, a user-defined function (UDF) was created to compute the necessary terms and add them to the momentum equation. The UDF scripts are written in a combination of C++ and a library of Fluent's own macro-functions (Ref. 28). Post-processing of the simulation data consisted of exporting pressure and shear stress data on the blade surface across 16 radial slices from Fluent. This data was then sorted in MATLAB and processed in Excel. An in-house BEMT code was used to compute reference values for comparison of sectional and integrated rotor loads against Fluent CFD results.

RESULTS

Knight & Hefner Rotor

The two-bladed Knight & Hefner rotor was simulated at blade collectives of 4°, 6°, 8°, and 10° at a constant rotational rate of $\Omega = 860$ RPM following the original report (Ref. 24). A small constant climb velocity of $V_C = 3m/s$ was added to ease the simulation and boundary-condition setup in ANSYS Fluent, corresponding to a climb ratio of $\lambda_c = 0.04$ practically close to hover conditions. The Knight & Hefner rotor characteristics used in this paper are displayed in Table 1.

Table 1. Knight & Hefner Rotor Characteristics.

Ω $[RPM]$	V_C $[m/s]$	Radius $[m]$	N_b	θ_{75} $[°]$	λ_c
860	3	0.765	2	4-10	0.04

Figure 4 shows sectional thrust and torque for the 6° collective, $V_C = 3m/s$ simulation, with CFD results from Fluent shown in black and BEMT reference values in gray. Note that results shown are thrust trimmed by adjusting the BEMT collective for this case to 5.92°. As for sectional thrust, the typical behavior of BEMT overpredicting tip loads when compared to CFD (Fluent) is visible; as for sectional torque, BEMT underpredicts along the blade with an overall underprediction of rotor power by only 2.5%. Therefore, blade sectional loads in Fig. 4 are considered in close enough agreement to test the proposed rotor force/power breakdown in the Fluent CFD analyses using the PPF methodology.

Figure 5 contains the sectional induced and profile torques for the same simulation. The CFD solution data (Fluent) based on solved static pressure or skin friction are displayed in black, and the BEMT reference values for induced or profile data in gray. Note that BEMT Eq. (18) was used here to generate the reference values for induced and profile torque. The aforementioned CFD technical barrier is evident when looking at the black and gray curves in Figure 5. In the left plot, static pressure torque from the CFD (Fluent) is not able to capture the induced torque because it also contains the form drag; in the right plot, the torque due to skin friction underpredicts the BEMT profile torque because it is missing the contribution from the form drag. This signifies the inherent limitation with current high-fidelity CFD solutions, i.e. individual sources of drag/power cannot be separated from the CFD solution. However, the PPF decomposition into Euler and dissipative partial pressures is able to break out the individual components from a viscous CFD solution following Eq. (9). Specifically, the Euler PPF, displayed by the black dots in the left plot of Figure 5, is able to extract the induced torque from the CFD solution and is in agreement with the BEMT reference values. The black dots in the sectional profile torque plot on the right are comprised of the contributions of skin friction and form drag, which is stored in the dissipative PPF according to Eq. (9). One can see that the dissipative PPF added to the skin friction contribution is able to capture the profile torque in the CFD (Fluent) and is in agreement with the BEMT reference values. This is the first time that rotor induced and profile torque were extracted from a converged CFD solution for a rotor in a slow climb using the PPF method of force/power breakdown.

Figure 6 contains the integrated rotor total, induced, and profile torques plotted against integrated rotor total thrust. As shown in the top plot, integrated rotor torque values from the simulations are in good agreement with the reference BEMT values. The middle plot reiterates the current technical barrier with modern CFD methods and the static pressure torque overpredicting the induced torque at every collective. Induced CFD torque in Fluent, however, captured in the Euler PPF, is in good agreement with the reference BEMT induced torque. The plot on the bottom of Figure 6 shows the Fluent skin friction torque underpredicting the reference BEMT profile torque. However, when the CFD form drag in Fluent, stored in the dissipative PPF, is added with the contribution of skin friction, one can capture the profile torque in a CFD solution.

Figure 7 shows distributions of static (c_p) and Euler (c_{p_E}) pressure coefficients at three different rotor blade sections at 6° collective and $V_C = 3m/s$. It can be seen that both pressure distributions are very similar; this is expected as the Euler PPF is interpreted as the equivalent inviscid pressure distribution extracted from the a full viscous CFD solution. In particular, it is evident that almost all blade section lift, and consequently induced drag (or drag due to lift), is captured in the Euler PPF (c_{p_E}) pressure coefficient. This supports that the Euler PPF behaves as expected by its theoretical formulation. Figure 8 shows distributions of corresponding dissipative pressure coefficient (c_{p_μ}) at the same three rotor blade sections. Note that the dissipative PPF is simply the difference between static pressure and the Euler PPF according to Eq. (2). As expected, the magnitude of the dissipative pressure coefficient (c_{p_μ}) is much smaller than that of the Euler pressure coefficient and only amount to a small percent of stagnation pressure. One important observation though is that c_{p_μ} is higher on the fore compared to the aft part of the local blade section, thereby resulting in a net form drag component of profile drag when locally integrated at a section of blade.

Table 2 summarizes results obtained for the two-bladed Knight & Hefner rotor. Note that blade collective is trimmed in the BEMT, see column 'Trim. Coll.', to obtain the same rotor thrust as for the CFD in Fluent. Rotor power agrees within just a few percent between Fluent and BEMT, with the largest

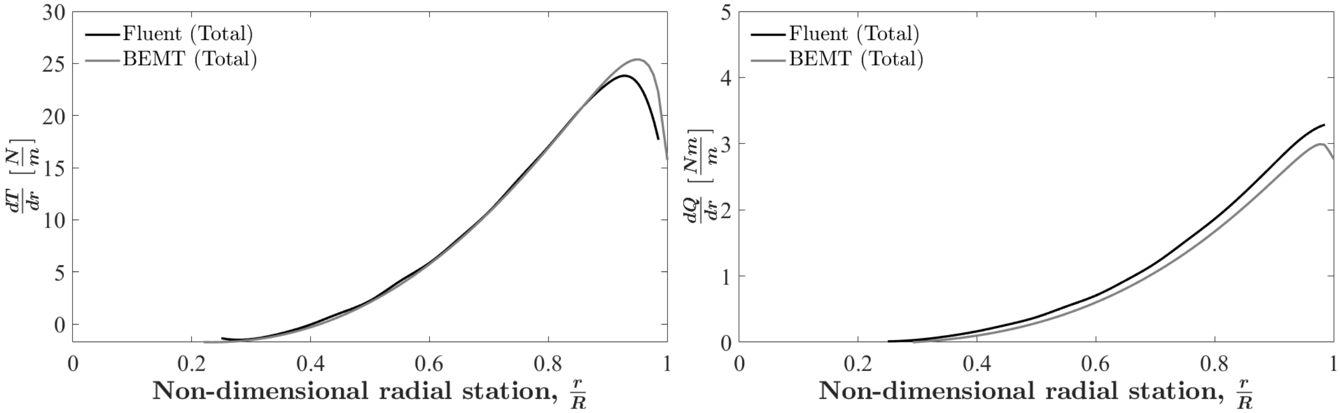

Figure 4. Knight & Hefner Rotor - Sectional Thrust and Torque (6° Collective, $V_C = 3m/s$, and 860 RPM).

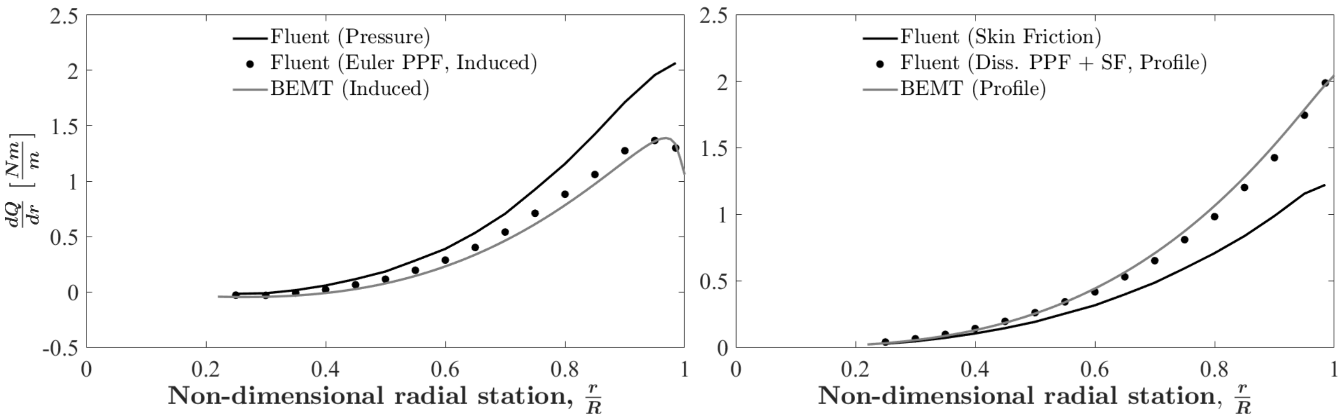

Figure 5. Knight & Hefner Rotor - Sectional Induced and Profile Torque (6° Collective, $V_C = 3m/s$, and 860 RPM).

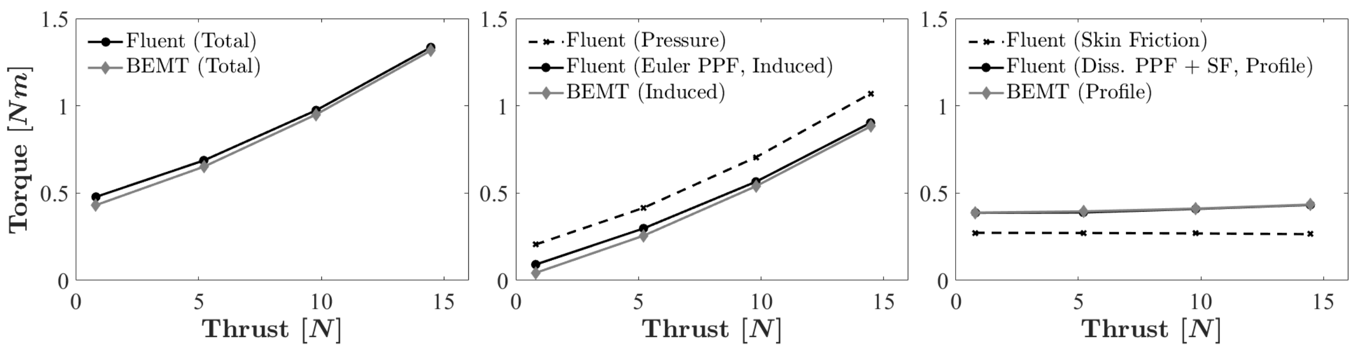

Figure 6. Knight & Hefner Rotor - Integrated Torque vs. Thrust Plots ($V_C = 3m/s$ and 860 RPM).

discrepancy occurring at the lowest blade collective. Also shown in Table 2 are induced and profile power for both Fluent and BEMT as reference values. It can be seen that induced and profile power extracted from Fluent by means of the PPF force/power breakdown agree very well with the BEMT reference values, with differences corresponding to those seen for total rotor power. Results obtained for profile power agree very well between Fluent and BEMT. Also shown are Fluent values for pressure and respective skin friction power (two most right columns in gray). One can see here how the pressure power overpredicts the induced power at each collective due to the contribution of the form drag. The inverse problem is seen again when comparing the skin friction power to the BEMT profile power. It is evident that when the contribution of the form drag, stored in the dissipative PPF, is removed from the static pressure power and added with the skin friction

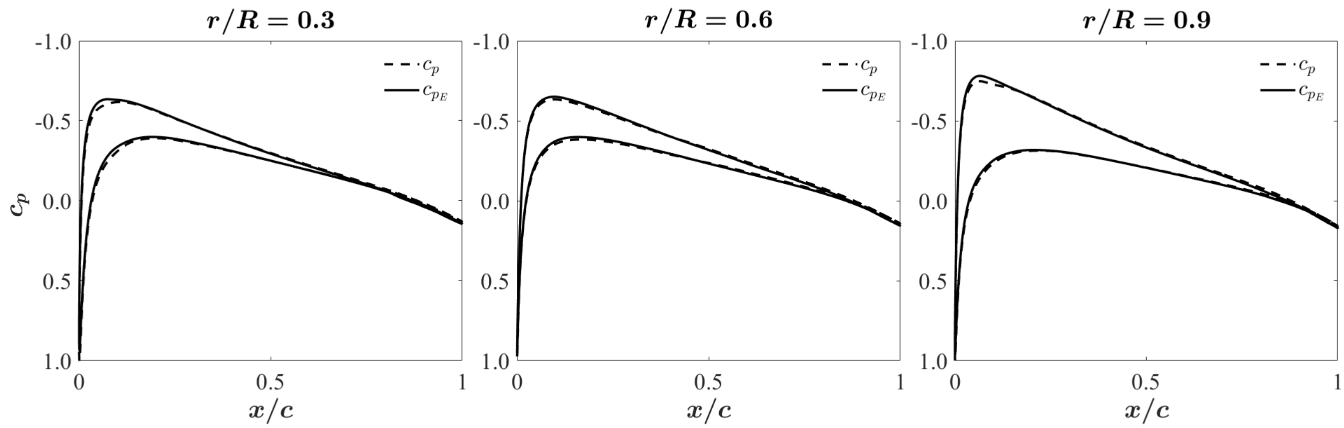

Figure 7. Knight & Hefner Rotor - Static c_p vs. Euler c_{p_E} pressure (6° Collective, $V_C = 3m/s$, and 860 RPM).

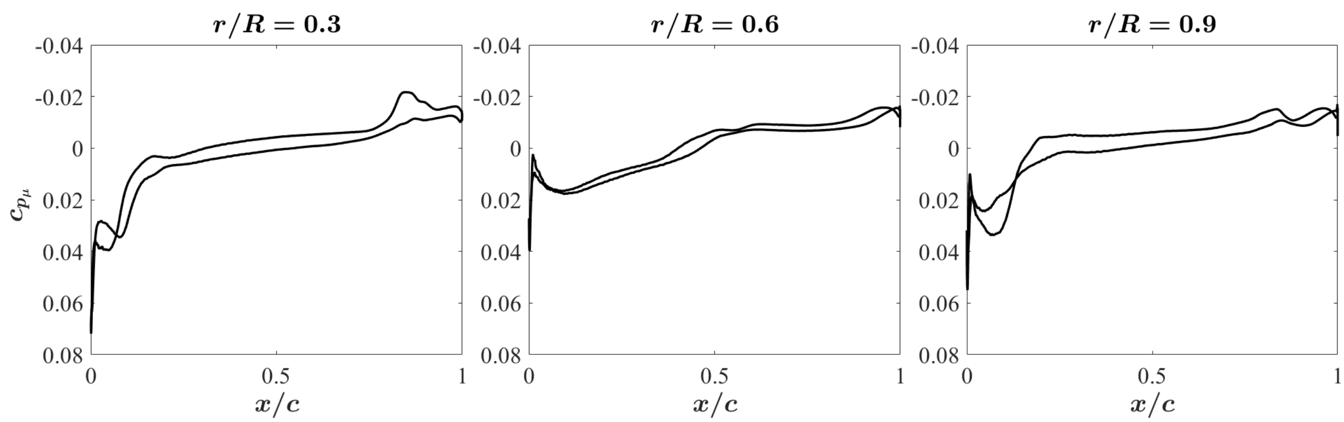

Figure 8. Knight & Hefner Rotor - Dissipative pressure c_{p_μ} (6° Collective, $V_C = 3m/s$, and 860 RPM).

Table 2. Knight & Hefner Rotor - Integrated Rotor Powers ($V_C = 3m/s$ and 860 RPM).

Blade Coll. [°]	Trim Coll. [°]	BEMT Power $[W]$	Fluent Power $[W]$	BEMT Ind. Power $[W]$	Fluent Ind. Power $[W]$	BEMT Prof. Power $[W]$	Fluent Prof. Power $[W]$	Fluent Press. Power $[W]$	Fluent Frict. Power $[W]$
4.0	3.96	77.62	86.08	7.744	16.39	69.88	69.70	37.10	48.58
6.0	5.92	117.2	123.7	46.10	53.66	71.14	70.06	74.74	48.80
8.0	7.76	171.1	175.4	97.08	101.8	74.02	73.66	127.0	48.44
10.0	9.52	237.2	240.4	159.0	162.5	78.16	77.80	192.7	47.72

contribution, one captures profile power while the Euler PPF captures the induced power of the rotor.

ONERA HAD-1 Propeller

The ONERA HAD-1 propeller was simulated in cruise ($M_\infty =$ 0.3) at a rotational rate of 2031 RPM in standard sea-level conditions according to (Ref. 11). The three-bladed propeller has a radius of $0.8m$ with a root-cutout of 15%. Some basic propeller characteristics are summarized in Table 3.

Table 3. ONERA HAD-1 Propeller Characteristics.

Ω $[RPM]$	M_∞	Radius $[m]$	N_b	θ_{75} [°]	J
2031	0.3	0.8	3	-45	0.6

All CFD simulations were conducted in Fluent and validated against CFD results obtained at ONERA (Ref. 11). A comparison of integrated thrust, torque, and power between Fluent and ONERA results is summarized in Table 4. The simulation from Fluent yielded less than a 2% difference in thrust and less than a 1% difference in torque which serves as very good validation of the Fluent results of the present work. A visualization of the propeller wake in the Fluent CFD simulations using the Q criterion is shown in Fig. 9.

Table 4. ONERA HAD-1 Propeller - CFD Validation.

Source	Thrust $[N]$	Torque $[Nm]$	Power $[kW]$
ONERA	1390	772.9	164.4
Fluent	1372	766.6	163.0
Δ [%]	1.33	0.83	0.83

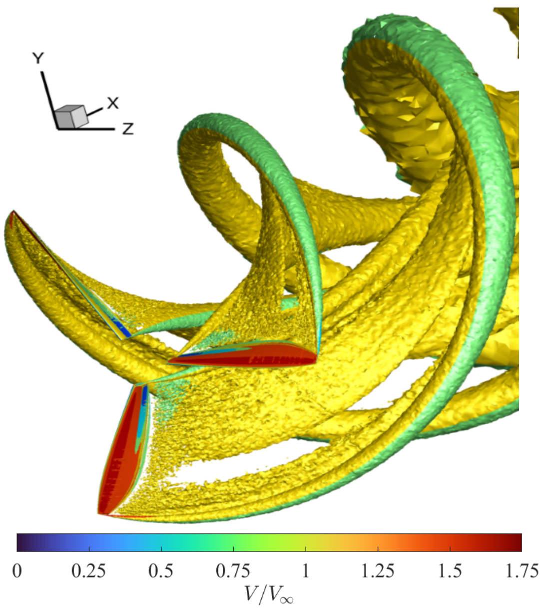

Figure 9. ONERA HAD-1 Propeller - Q-Criterion Iso-Surface ($M_\infty = 0.3$ and 2031 RPM).

As for the BEMT inflow Eq. (27) used for the ONERA HAD-1 propeller, the computed induced velocity, v_i, at the rotor blade was compared to an actuator-line model result from (Ref. 29) as a validation case. It can be seen in Fig. 10 that comparisons are quite good, albeit noting that this is not an accurate model-to-model comparison; nonetheless, it supports the validity of BEMT computed inflow for this case.

The plots in Fig. 11 show blade sectionional thrust and torque for the ONERA HAD-1 propeller case. As in the Knight & Hefner section, CFD results from Fluent are shown in black and BEMT reference values in gray. The BEMT blade collective was trimmed to match the Fluent CFD computed thrust. As for sectional thrust in Fig. 11, the CFD (Fluent) and BEMT results match closely, with the BEMT underpredicting inboard and overpredicting in the tip region as is typically observed. Note again that the integrated thrust $T = 1372N$ is the same for both cases. As far as sectional torque is concerned, CFD results from Fluent and BEMT reference values agree quite well, with a small BEMT underprediction along the blade (except for the tip region), accounting for only a 5% difference in integrated rotor torque and power. Therefore,

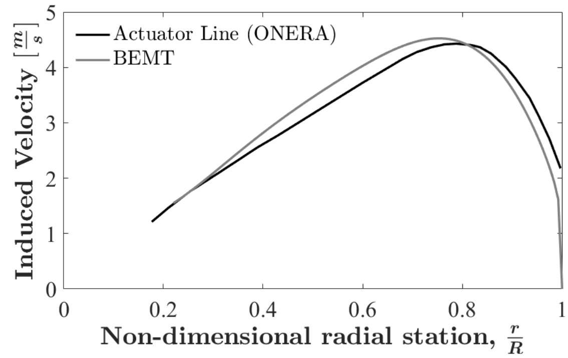

Figure 10. BEMT - Induced Velocity Comparison (Ref. 29)

the comparisons are considered very good and suitable for a subsequent breakdown of the Fluent CFD rotor power into induced and profile contributions and comparison to BEMT reference values.

The left plot in Fig. 12 shows sectional induced torque. One can see that the black line, representing Fluent CFD pressure torque, overpredicts the BEMT induced torque because it contains the contribution of form drag. The technical barrier with modern CFD methods is evident again. However, upon extracting the form drag using the dissipative PPF, the Euler partial pressure represented by the black dots captures the induced torque and matches well with the reference BEMT induced torque for the inboard portion of the blade. In the right plot in Fig. 12, the Fluent CFD computed skin friction underpredicts BEMT profile torque as it does not include the form drag component associated with the dissipative partial pressure; however, when added to the skin friction, the Fluent CFD profile torque, shown as black dots, overpredicts compared to the BEMT reference value for profile torque. As will be discussed below with tabulated data, the aforementioned 5% discrepancy between Fluent CFD and BEMT is almost entirely captured in this difference in profile torque and can be reasonably attributed to additional three-dimensional effects not captured by the BEMT for the highly-twisted ONERA HAD-1 propeller. While seemingly small from the viewpoint of overall quantitative comparison, it is nonetheless notable for this case where profile power is only about 3% of total rotor power and therefore does not necessarily allude to shortcomings in the proposed PPF force/power decomposition method. For comparison, profile power of the Knight & Hefner rotor as shown in Table 2 is upwards of 50% for a simple geometry at significantly lower Reynolds number and disk loading compared to the ONERA HAD-1 propeller.

Table 5 summarizes the results obtained on the ONERA HAD-1 propeller and associated breakdown into rotor induced and profile power. Note that the blade collective in the BEMT was trimmed to match integrated rotor thrust in the Fluent CFD simulation. Rotor power agrees to within 5% (or $8kW$) between both methods. As for rotor induced power, Fluent CFD and BEMT agree to within 1.5%. This can be regarded very good agreement and supports the proposed rotor force/power decomposition using the Euler PPF; note that

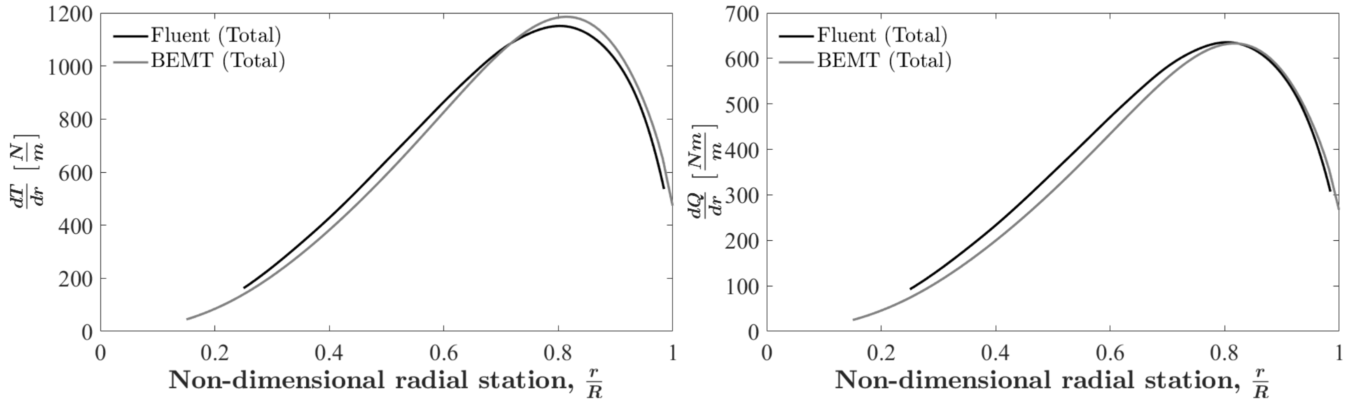

Figure 11. ONERA HAD-1 Propeller - Sectional Thrust and Torque ($M_\infty = 0.3$ and 2031 RPM).

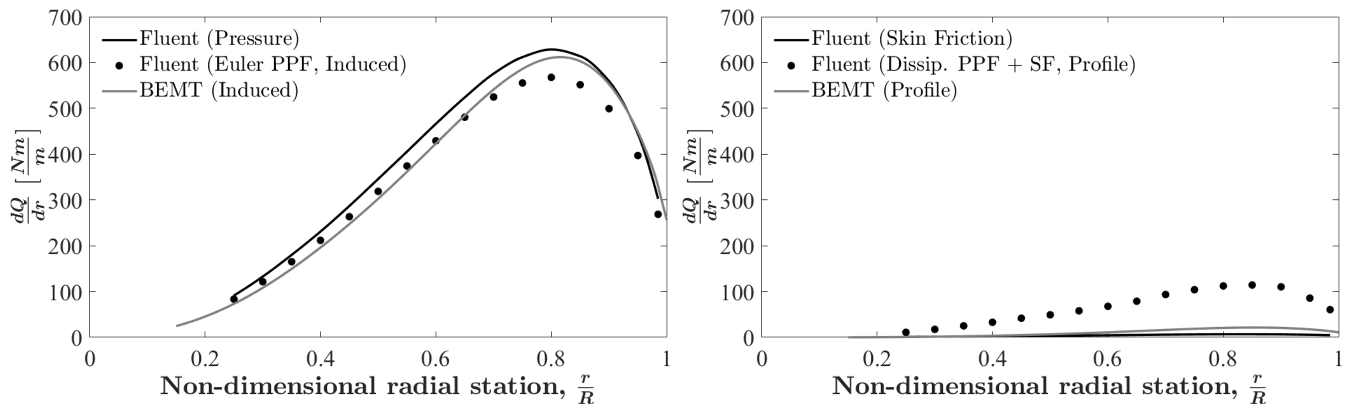

Figure 12. ONERA HAD-1 Propeller - Sectional Induced and Profile Torque ($M_\infty = 0.3$ and 2031 RPM).

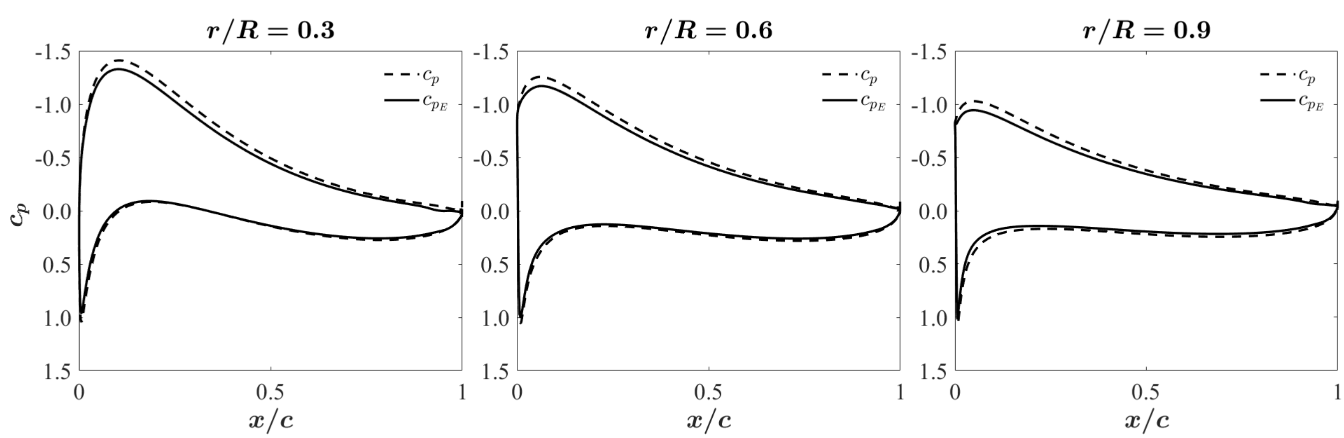

Figure 13. ONERA HAD-1 Propeller - Static c_p vs. Euler c_{p_E} pressure ($M_\infty = 0.3$ and 2031 RPM).

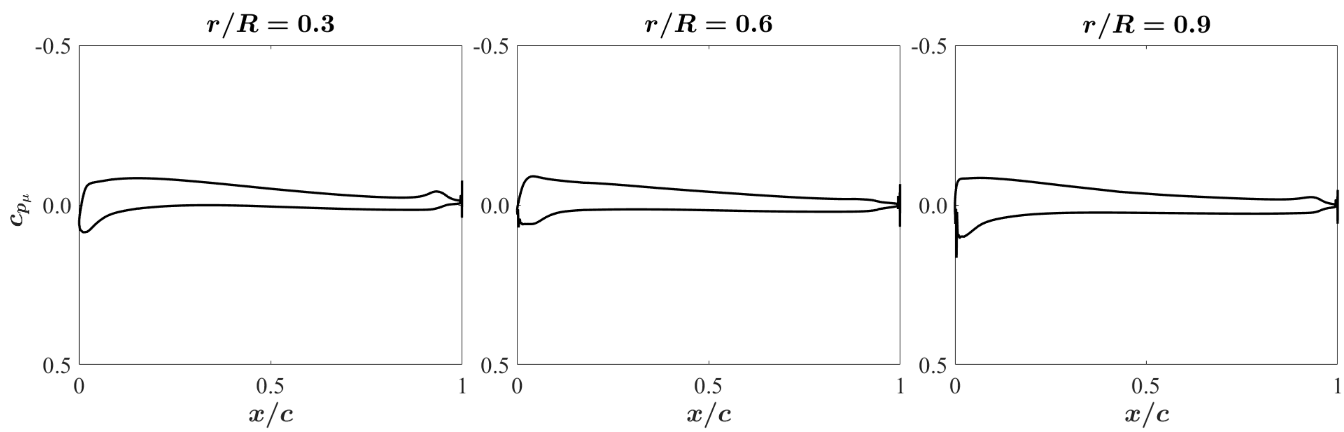

Figure 14. ONERA HAD-1 Propeller - Dissipative pressure c_{p_μ} ($M_\infty = 0.3$ and 2031 RPM).

Table 5. ONERA HAD-1 Propeller - Integrated Rotor Powers ($M_\infty = 0.3$ and 2031 RPM).

Blade Pitch [°]	Trim Pitch [°]	BEMT Power $[kW]$	Fluent Power $[kW]$	BEMT Ind. Power $[kW]$	Fluent Ind. Power $[kW]$	BEMT Prof. Power $[kW]$	Fluent Prof. Power $[kW]$	Fluent Press. Power $[kW]$	Fluent Frict. Power $[kW]$
47.0	45.2	155.1	163.0	150.5	148.1	4.482	15.95	161.2	1.833

the Fluent CFD pressure power (shown in gray in Table 5) is by itself higher than the total BEMT rotor power. Results appear to be also consistent insofar as the Fluent CFD friction power (most right column in gray) underpredicts BEMT profile power as it is missing the sectional form drag component. As far as rotor profile power is concerned, the difference between Fluent CFD and BEMT is more pronounced and corresponding closely to the overall difference in rotor power of approximately $8kW$; this is attributed to additional three-dimensional effects not captured in the BEMT in general and might also be a result of the difference in trimmed pitch angle of 1.8° as seen in Table 5 being notably larger than for the simpler Knight & Hefner rotor planform (see Table 2).

Figure 13 shows distributions for static (c_p) and Euler (c_{p_E}) pressure coefficients at three different radial stations along the propeller blade. Similarly as observed earlier for the Knight & Hefner rotor, pressure distributions are quite similar, which is expected from the theory of the Euler partial pressure representing the inviscid pressure extracted from the full viscous Fluent CFD solution. It is notable though that differences are more pronounced than for the Knight & Hefner rotor. This is evident when looking at the dissipative pressure coefficient (c_{p_μ}) in Fig. 14 showing higher values than observed for the Knight & Hefner rotor. Here it is again conjectured that for the ONERA HAD-1 propeller, additional three-dimensional effects are present due to the relatively complex blade planform geometry of the highly-twisted propeller blade and that those are captured in the dissipative PPF from Fluent CFD. This is consistent with the tabulated values in Table 5.

CONCLUSIONS

The current technical barrier of being unable to accurately extract rotor induced and profile power from high-fidelity CFD solutions has not been overcome due to the fact that the CFD computed static pressure contributes to both induced power and also includes the form drag component of profile power.

The contribution of this paper is a novel methodology that enables extracting rotor induced and profile power from high-fidelity CFD simulations, thereby removing this fundamental technical barrier. The method is based on the theory of partial-pressure fields that have been successfully applied to aircraft drag decomposition in previous work. The present work extends the proven concept to rotating reference frames.

The proposed partial-pressure field (PPF) force/power breakdown for rotorcraft applications was demonstrated for two different rotors: i) the 2-bladed Knight & Hefner rotor (incompressible flow) and ii) the ONERA HAD-1 propeller (compressible flow). For both test cases, BEMT was used to generate reference values for comparison against induced and profile power extracted from high-fidelity CFD in Fluent.

A summary of this paper's main results are listed below:

1. Extracting induced and profile power from a viscous rotorcraft CFD solution is possible using the near-field Euler & dissipative PPF force/power breakdown method.

2. For both rotors, CFD extracted induced power compares to within a few percent [%] to BEMT reference values.

3. The CFD extracted profile power includes additional three-dimensional effects not captured by BEMT.
4. The Euler & dissipative PPFs can be readily solved from a converged viscous CFD solution using either a general transport equation or Poisson solver.

The results obtained in this work are potentially impactful to the rotorcraft community inasmuch the method holds promise for future developments to also accurately extract airfoil polar data and tip-loss factors from the CFD with the intent to improve current low-fidelity BEMT methods.

Author contact: Albert Abraham aja387@psu.edu
Pierce Hart puh69@psu.edu
Sven Schmitz sus52@psu.edu

ACKNOWLEDGMENTS

This research is funded by the Government under Cooperative Agreement No. W911W6-21-2-0002. The U.S. Government is authorized to reproduce and distribute reprints for Government purposes notwithstanding any copyright notation thereon. The views and conclusions contained in this document are those of the authors and should not be interpreted as representing the official policies or position, either expressed or implied, of the U.S. Army Combat Capabilities Development Command (DEVCOM), Aviation & Missile Center (AvMC), or the U.S. Government. The authors would like to thank Rohit Jain, Mani Ramasamy, and Mahendra Bhagwat of the U.S. Army DEVCOM Aviation & Missile Center for their insights and feedback throughout this project. The authors are grateful to ONERA (Contact: Dr. Ilias Petropoulos) for providing the CAD reference geometry of the ONERA HAD-1 propeller in support of numerical investigations in the field of force/power breakdown and energy/exergy analysis methods.

REFERENCES

1. Berton, J., "Design of an Open Rotor, Braced-Wing Electric Transport," Technical report, NASA/TM-20220015470, 2022.
2. Oswatitsch, K., "Der Luftwiderstand als Integral des Entropiestromes," *Nachrichten der Akademie der Wissenschaften in Göttingen, Mathematisch-Physikalischer Klasse*, Vol. 19, 1945, pp. 88–90.
3. van der Vooren, J., and Slooff, J., *CFD-based Drag Prediction: State-of-the-art, Theory, Prospects*, Nationaal Lucht- en Ruimtevaartlaboratorium, NLR, Ansterdam, 1992.
4. Paparone, L., and Tognaccini, R., "Computational Fluid Dynamics-Based Drag Prediction and Decomposition," *AIAA Journal*, Vol. 41, (9), 2003, pp. 1647–1657. DOI: 10.2514/2.7300.
5. Destarac, D., and Vooren, J., "Drag/Thrust Analysis of Jet-Propelled Transonic Transport Aircraft; Definition of Physical Drag Components," *Aerospace Science and Technology*, Vol. 8, September 2004, pp. 545–556. DOI: 10.1016/j.ast.2004.03.004.
6. Verley, S., *Évaluation du couple "champ lointain" d'un rotor d'hélicoptère en vol stationnaire: analyse de résultats issus de simulations numériques de mécanique des fluides*, Ph.D. thesis, Université d'Orléans, France, Last Accessed: 06.25.2025, 2012.
7. Meheut, M., "Thrust and Torque Far-field Analysis of Propeller and Counter Rotating Open Rotor Configurations," Paper AIAA 2013-2803, 31st AIAA Applied Aerodynamics Conference, San Diego, CA, June 24–27, 2013. DOI: 10.2514/6.2013-2803.
8. Gariepy, M., Trepanier, J.-Y., and Malouin, B., "Generalization of the Far-Field Drag Decomposition Method to Unsteady Flows," *AIAA Journal*, Vol. 51, (6), 2013, pp. 1309–1319. DOI: 10.2514/1.J051609.
9. Toubin, H., and Bailly, D., "Development and Application of a New Unsteady Far-Field Drag Decomposition Method," *AIAA Journal*, Vol. 53, (11), 2015, pp. 3414–3429. DOI: 10.2514/1.J054002.
10. Toubin, H., Bailly, D., and Costes, M., "Improved Unsteady Far-Field Drag Breakdown Method and Application to Complex Cases," *AIAA Journal*, Vol. 54, (6), 2016, pp. 1907–1921. DOI: 10.2514/1.J054756.
11. Nadal, M., Fournis, C., and Lewis, D., "Unsteady Far-Field Drag Analyses of the ONERA HAD-1 Propeller," Paper AIAA 2024-4345, AIAA Aviation Forum and ASCEND Conference, Las Vegas, NV, July 29 – August 2 2024. DOI: 10.2514/6.2024-4345.
12. Arntz, A., *Civil Aircraft Aero-thermo-propulsive Performance Assessment by an Exergy Analysis of High-fidelity CFD-RANS Flow Solutions*, Ph.D. thesis, Université de Lille 1, France, Last Accessed: 06.25.2025, 2014.
13. Arntz, A., and Hue, D., "Exergy-Based Performance Assessment of the NASA Common Research Model," *AIAA Journal*, Vol. 54, (1), 2016, pp. 88–100. DOI: 10.2514/1.J054127.
14. Arntz, A., and Atinault, O., "Exergy-Based Performance Assessment of a Blended Wing–Body with Boundary-Layer Ingestion," *AIAA Journal*, Vol. 53, (12), 2015, pp. 3766–3776. DOI: 10.2514/1.J054072.
15. Berhouni, I., Bailly, D., and Petropoulos, I., "Exergy Balance Extension to Rotating Reference Frames: Application to a Propeller Configuration," *AIAA Journal*, Vol. 61, (4), 2023, pp. 1790–1806. DOI: 10.2514/1.J062216.

16. Berhouni, I., Petropoulos, I., and Bailly, D., "Decomposition of Compressible and Thermal Contributions to the Exergy-Balance-Based Analysis of the NASA Rotor 37," ASME Turbo Expo 2024: Turbomachinery Technical Conference and Exposition, London, UK, June 24–28 2024. DOI: 10.1115/GT2024-120925.

17. Morelli, M., Trapier, S., Vega, L., Thollet, W., Petropoulos, I., and Berhouni, I., "Assessment of the Far-Field Exergy Balance Method for Industrial Aerodynamic and Aerothermal Applications," Paper AERO2024-37, 58th 3AF International Conference on Applied Aerodynamics, Orléans, France, March 27–29 2024.

18. Schmitz, S., and Coder, J. G., "Inviscid Circulatory-Pressure Field Derived from the Incompressible Navier–Stokes Equations," *AIAA Journal*, Vol. 53, (1), 2015, pp. 33–41. DOI: 10.2514/1.J053140.

19. Schmitz, S., "Drag Decomposition Using Partial-Pressure Fields in the Compressible Navier–Stokes Equations," *AIAA Journal*, Vol. 57, (5), 2019, pp. 2030–2038. DOI: 10.2514/1.J057701.

20. Hart, P. L., and Schmitz, S., "Drag Decomposition Using Partial-Pressure Fields: ONERA M6 Wing," *AIAA Journal*, Vol. 60, (5), 2022, pp. 2941–2952. DOI: 10.2514/1.J061152.

21. Hart, P. L., and Schmitz, S., "Partial Pressure Field for Airfoil Wave Drag," *AIAA Journal*, Vol. 60, (10), 2022, pp. 5791–5804. DOI: 10.2514/1.J061690.

22. Hart, P. L., Axten, C. J., Maughmer, M. D., and Schmitz, S., "Drag Decomposition Using Partial-Pressure Fields: Ventus-3 and NASA Common Research Model," *Journal of Aircraft*, Vol. 60, (6), 2023, pp. 1798–1810. DOI: 10.2514/1.C037325.

23. Hart, P. L., Vogel, A., Bradley, F., and Schmitz, S., "A Near-field CFD Method for Wave Drag Decomposition," Paper AIAA 2025-3430, AIAA Aviation Forum and ASCEND Conference, Las Vegas, NV, July 21–25 2025. DOI: 10.2514/6.2025-3430.

24. Montgomery, K., and Hefner, R. A., "Static Thrust Analysis of the Lifting Airscrew," Technical report, NACA Technical Note 626, 1937.

25. Leishman, J. G., *Principles of Helicopter Aerodynamics*, Cambridge University Press, New York, NY, second edition, 2006, Chapter 3.

26. McCormick, B. W., *Aerodynamics, Aeronautics, and Flight Mechanics*, John Wiley & Sons, New York, NY, second edition, 1994, Chapter 6.

27. Schmitz, S., *Aerodynamics of Wind Turbines: A Physical Basis for Analysis and Design*, John Wiley & Sons, Hoboken, NJ, 2020, Chapter 3.

28. *ANSYS Fluent Customization Manual*, ANSYS, 2022, [retrieved 09/02/2022].

29. Pantel, H., Falissard, F., and Dufour, G., "Assessment of Reynolds-Averaged Navier-Stokes/Blade Element Theory Body Force Method for Propeller Modeling," *AIAA Journal*, Vol. 62, (2), 2023, pp. 758–775. DOI: 10.2514/1.J063302.